

# UC Riverside

## UC Riverside Previously Published Works

**Title**

Near-Infrared-Fluorescent Erythrocyte-Mimicking Particles: Physical and Optical Characteristics

**Permalink**

<https://escholarship.org/uc/item/01k029n8>

**Journal**

IEEE Transactions on Biomedical Engineering, 66(4)

**ISSN**

0018-9294

**Authors**

Tang, Jack C  
Partono, Allen  
Anvari, Bahman

**Publication Date**

2019-04-01

**DOI**

10.1109/tbme.2018.2866368

Peer reviewed

# Near-Infrared-Fluorescent Erythrocyte-Mimicking Particles: Physical and Optical Characteristics

Jack C. Tang, Allen Partono, and Bahman Anvari

**Abstract**—Exogenous fluorescent materials activated by near-infrared (NIR) light can offer deep optical imaging with sub-cellular resolution, and enhanced image contrast. We have engineered NIR particles by doping hemoglobin-depleted erythrocyte ghosts (EGs) with indocyanine green (ICG). We refer to these optical particles as NIR erythrocyte-mimicking transducers (NETs). A particular feature of NETs is that their diameters can be tuned from micrometer to nanometer scale, thereby, providing a capability for broad NIR biomedical imaging applications. Herein, we investigate the effects of ICG concentration on key material properties of micrometer-sized NETs, and nanometer-sized NETs fabricated by either sonication or mechanical extrusion of EGs. The zeta potentials of NETs do not vary significantly with ICG concentration, suggesting that ICG is encapsulated within NETs regardless of particle size or ICG concentration. Loading efficiency of ICG into the NETs monotonically decreases with increasing values of ICG concentration. Based on quantitative analyses of the fluorescence emission spectra of the NETs, we determine that 20  $\mu\text{M}$  ICG utilized during fabrication of NETs presents an optimal concentration that maximizes the integrated fluorescence emission for micrometer- and nanometer-sized NETs. Encapsulation of ICG in these constructs also enhanced the fluorescence stability and quantum yield of ICG. These results guide the engineering of NETs with maximal NIR emission for imaging applications such as fluorescence-guided tumor resection, and real-time angiography.

**Index Terms**— biomedical optical imaging, biomembranes, biomimetic materials, biophotonics, molecular imaging, nanobiotechnology, nanomedicine, particle production.

## I. INTRODUCTION

Use of exogenous fluorescent materials activated by near-infrared (NIR) excitation provides a capability for deep, high-resolution biomedical optical imaging at the cellular and molecular levels [1, 2]. These advantages are primarily due to reduced light absorption and scattering by hemoglobin, water, and other biological components in the NIR transparency window [3, 4]. Additionally, exogenous

fluorescent materials that emit in this window can enhance the imaging contrast as a result of reduced autofluorescence by endogenous fluorophores in this spectral band [1]. Thus, high signal to noise, and deep optical penetration, on the order of at least about one cm, can be achieved by NIR imaging [1, 5].

One NIR-fluorescent contrast agent of immense interest is indocyanine green (ICG). It remains as the only FDA-approved NIR fluorophore for specific applications including assessment of cardiac output [6, 7], hepatic function [8-10], retinal angiography [11-13]. Having been used in thousands of patients with rare occurrence of side effects ( $<0.15\%$ ) [14], ICG is considered to be one of the least toxic agents administered in humans [1]. ICG has also been used for non-FDA-approved investigational applications, such as sentinel lymph node biopsy [15-23], photothermal therapy [24-26], and photodynamic therapy [26-30]. ICG-based fluorescence angiography for vascular mapping and perfusion assessment is also becoming increasingly attractive [31-35], without the drawbacks of potential toxicity or radioactivity of some of the contrast agents associated with CT and MR angiography.

In recent years, a number of fluorescence imaging systems have been developed for use with ICG. Several of these systems have reached preclinical or clinical stages, including the Curadel FLARE, Novadaq Spy Elite, Hamamatsu PDE-NEO II, Fluoptics Fluobeam, Intuitive Surgical da Vinci Firefly, and Nawoo Vision FIAT-L imaging systems [36, 37], further emphasizing the growing interest in NIR fluorescence imaging, particularly based on ICG.

Nevertheless, despite its established clinical utility, a disadvantage of ICG is its short circulation half-life ( $\approx 2$ -4 minutes) [38, 39]. Upon intravenous injection, ICG non-specifically binds to serum proteins, such as albumin, and is uptaken by hepatocytes [40-42]. One strategy for extending the circulation half-life of ICG is to encapsulate the dye into protective constructs. Encapsulation can also serve to enhance the stability of ICG, which can degrade due to heat or optical exposure [43, 44]. To date, various materials have been used to encapsulate ICG, including polymers [45, 46], plant-virus capsids [47-49], and liposomes [50, 51].

Encapsulation of ICG into liposomes has been shown to increase the fluorescence quantum yield of ICG [43, 52]. However, liposomal formulation lacks the presence of immunomodulatory surface proteins that may be required to increase the circulation time of ICG. For example, the reported half-life of ICG in liposomal nanoparticles following intravenous injection in mice is less than a minute [53].

Submitted for review on March 24, 2018. This work was supported in part by grants from the National Science Foundation (CBET-1509218), National Institute of Arthritis and Musculoskeletal and Skin Diseases (R01-AR068067), and National Cancer Institute (1R43-CA210715).

J. C. Tang, A. Partono, and B. Anvari are with the Department of Bioengineering, University of California, Riverside, Riverside, CA, USA (correspondence email: anvarib@ucr.edu).

Copyright (c) 2017 IEEE. Personal use of this material is permitted. However, permission to use this material for any other purposes must be obtained from the IEEE by sending an email to [pubs-permissions@ieee.org](mailto:pubs-permissions@ieee.org).

Recently, we have encapsulated ICG using hemoglobin-depleted red blood cells (RBCs), also known as erythrocyte ghosts (EGs) [54-57]. We refer to these ICG loaded particles as NIR erythrocyte-mimicking transducers (NETs) since they can use NIR light to generate heat, fluorescence, and reactive oxygen species [58]. Several groups, including our own, have investigated NETs for imaging, phototherapeutic, and drug-delivery applications [55-57, 59-62]. EGs have been used to encapsulate and deliver other therapeutic and diagnostic payloads as well [63-65].

Native RBCs have long circulation times on the order of  $\approx 90$ -120 days, attributed in part to the presence of specific “self-marker” membrane proteins such as CD47, that allow them to evade immune cells [66]. We have previously demonstrated that CD47 can remain on the surface of NETs [56]; hence, providing a mechanism for extended circulation of NETs. As constructs that can be fabricated using autologous blood or compatible blood types, NETs may prove to be non-toxic materials for biomedical imaging and therapeutic applications.

A useful feature of NETs is that their diameter can be tuned to various sizes ranging from nanometer to micrometer scale, and that their ICG content can be adjusted during the fabrication process. Nanometer-sized NETs (nNETs) have relevance to cancer optical theranostics, based on the enhanced permeability and retention (EPR) effect [67, 68]. Micrometer-sized NETs ( $\mu$ NETs) may be useful for angiography, and photothermal treatment of vascular cutaneous diseases, such as the port wine stain.

In this study, we fabricated  $\mu$ NETs, and nNETs formed by two methods based on mechanical extrusion, and sonication. Our objective was to investigate the effects of changing the ICG concentration utilized during the fabrication process on the resulting material properties, including zeta potential, ICG loading efficiency, and optical absorption and fluorescence characteristics of both  $\mu$ NETs and nNETs. We also demonstrate that NETs can retain their fluorescence characteristics for at least up to 12 hours in storage (4 °C) and at physiological (37 °C) temperatures. The fluorescence characteristics are particularly important for clinical translation of NETs for biomedical fluorescence imaging, and provide the basis for selecting an optimized concentration of ICG that can produce  $\mu$ NETs and nNETs with maximal fluorescence emission.

## II. MATERIALS AND METHODS

### A. Formation of Micrometer-Sized Erythrocyte Ghosts ( $\mu$ EGs)

Intact RBCs were isolated from whole bovine blood (1 ml) (Rockland Immunochemicals, Inc., Limerick, PA, USA) in citrate by centrifugation ( $1000 \times g$ , 5 minutes, 4 °C) (Eppendorf 5424 Microcentrifuge, Hamburg, Germany). The supernatant containing the plasma and buffy coat was discarded, and the erythrocytes were re-suspended in 1 ml of  $\approx 300$  mOsm phosphate-buffered saline (1X PBS) (Fisher Bioreagents, Fair Lawn, New Jersey, USA). Erythrocytes were isolated by centrifugally washing them three times in 1X PBS ( $1000 \times g$ , 5 minutes, 4 °C).

To remove intracellular hemoglobin, the isolated RBCs were incubated in increasingly hypotonic conditions. Specifically, we incubated the RBCs for 20 minutes in 0.5X PBS (1 ml, 4 °C). These RBCs were then collected by centrifugation ( $20,000 \times g$ , 15 minutes, 4 °C), and the red supernatant (containing hemoglobin and other intracellular contents) was discarded. The pellet of these erythrocytes with partial hemoglobin depletion was then re-suspended in 1 ml of 0.5X PBS. This hypotonic treatment in 0.5X PBS was repeated a total of three times. Then, we decreased the tonicity of the buffer, and re-suspended the erythrocytes in 0.25X PBS and incubated them for 20 minutes at 4 °C. Then, the particles were centrifugally washed ( $20,000 \times g$ , 15 minutes, 4 °C). Hypotonic treatment and wash in 0.25X PBS was repeated a total of three times.

Hemoglobin-depleted EGs were then resealed by centrifugally washing the pellet in 1X PBS ( $20,000 \times g$ , 15 minutes, 4 °C), and re-suspending the pellet in 1X PBS. The resulting micrometer-sized EGs ( $\mu$ EGs) were diluted to have an absorbance value of two at 280 nm, corresponding to  $\approx 0.04$  ml of  $\mu$ EGs used for each 1 ml of NETs. The 280 nm wavelength corresponds to the absorption peak of the aromatic rings found in proteins, which enabled us to control the amount of EG material in each sample.

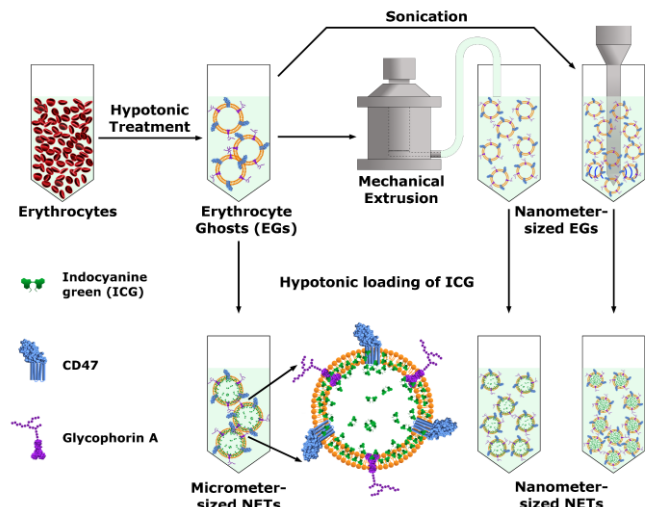


Fig. 1. Schematic of the processes to fabricate micrometer- and nanometer-sized NETs ( $\mu$ NETs and nNETs, respectively). After the formation of micrometer-sized erythrocyte ghosts ( $\mu$ EGs), these particles can be loaded with ICG to form  $\mu$ NETs.  $\mu$ EGs are mechanically extruded, or sonicated to reduce their size to the nanometer scale before loading with ICG to yield nNETs.

### B. Sonication and Mechanical Extrusion of EGs

We reduced the size of  $\mu$ EGs to the nanometer-scale using two methods: sonication and mechanical extrusion (Fig. 1). Under the sonication method,  $\mu$ EGs were subject to ultrasonic pulses for eight minutes (30 W, 20 kHz) using a Misonix S-400 probe sonicator (Farmingdale, NY, USA). Each pulse lasted 5 seconds, and pulses were delivered 20 seconds apart. To avoid heating of the EGs, the vial containing the solution was placed in a beaker of ice water during sonication. We replaced the ice after each minute of sonication. After every two minutes of sonication, the EGs were given five minutes to rest in fresh ice water. After sonication was completed, the nanometer-sized EGs (nEGs) were centrifugally washed

(100,000  $\times$  g, one hour, 4 °C) in a Type 90ti rotor (Beckman Coulter, Inc., Palo Alto, CA, USA) and re-suspended in 1X PBS.

Under the extrusion method,  $\mu$ EGs were sequentially extruded through track-etched polyester membranes (Sterlitech Corp., Kent, WA, USA) with defined pore diameters (800, 400, and 200 nm) to form nanometer-sized EGs (nEGs). EGs were passed through each size membrane at least three times. To prevent excessive clogging of the pores,  $\mu$ EGs were diluted ten-fold in 1X PBS prior to extrusion and re-concentrated afterwards. Extrusion was performed using a 10 ml LIPEX® extruder (TRANSFERRA Nanosciences Inc., Burnaby, B.C., Canada). Extruded nEGs were then centrifugally washed (100,000  $\times$  g, one hour, 4 °C), and re-suspended in their original volume of 1X PBS.

### C. Loading EGs with ICG to form NETs

Each type of EG (micrometer-, and nanometer-sized formed by sonication or extrusion) was loaded with ICG by incubating the EGs in a hypotonic solution containing ICG. The ICG loading buffer contained a 1:1:1 volume ratio of EGs, Sørensen's phosphate buffer (0.1 M, pH 7.4), and a known concentration of aqueous ICG. We varied the total concentration of the ICG loading buffer (0, 1, 5, 10, 20, 50, 75, and 100  $\mu$ M) and incubated the EGs with the indicated ICG loading buffers for 30 minutes to form NETs. The total tonicity of the ICG loading buffers was  $\approx$ 175 mOsm.

Following incubation, excess ICG was removed by centrifugation (20,000  $\times$  g, 15 minutes for  $\mu$ NETs; 100,000  $\times$  g, one hour for nNETs formed by sonication or extrusion). The supernatant was set aside to quantify the loading efficiency of ICG into NETs (as described below). The resulting NETs were then washed in 3 ml of 1X PBS to reseal the membranes and remove residual ICG. The supernatant from this wash was removed and added to the supernatant for quantification of the ICG loading efficiency of NETs. NETs were then re-suspended in 1 ml of 1X PBS for characterization studies.

### D. Dynamic Light Scattering-Based Measurement of NETs Diameters and Zeta Potential

The hydrodynamic diameters of each NETs formulation was measured by dynamic light scattering (DLS) using a Malvern Zetasizer NanoZS (Malvern, United Kingdom). Samples were suspended in 1 ml 1X PBS within a polystyrene cuvette (1 cm pathlength). Each DLS measurement was collected at a scattering angle of 90°. We report the size of NETs using the z-average diameter, which is the intensity-based harmonic mean of the light-scattering particles [69, 70]. Eight measurements were taken for each sample, and averaged. The average diameters of three independent samples were then used to calculate the mean z-average diameter and the corresponding standard deviation (SD).

The zeta potential ( $\zeta$ ) of NETs and EGs in 1X PBS were also estimated using the Malvern Zetasizer via the Smoluchowski approximation, which relates the  $\zeta$  to the observed electrophoretic mobility of the particles [71, 72]. Each measurement was done in a folded capillary cell at 10 °C. Similar to the z-average diameter characterizations, the  $\zeta$  of each formulation of NETs was measured eight times, and

averaged. This was done for three independent samples, and used to estimate the mean  $\zeta$  and the corresponding SD.

### E. Fluorescence Microscopy of $\mu$ NETs

Fluorescence images of  $\mu$ NETs were obtained using a Hamamatsu C9100-13 electron-multiplying charge-coupled detector (Hamamatsu, Japan) with a Nikon Eclipse Ti microscope (Tokyo, Japan) and a Chroma Li-Cor IR800 filter cube (Bellows Falls, Vermont, USA). We used a Nikon oil-immersion objective lens with 100x magnification (Tokyo, Japan). The excitation band was  $740 \pm 20$  nm, and the emission was passed through a filter transmitting wavelengths greater than 780 nm.

### F. UV-Vis-NIR Absorption Spectra of NETs

Steady-state absorption spectrum of each formulation of NETs was recorded using a UV-Vis-NIR spectrophotometer (JASCO V-670, Tokyo, Japan) in transmission mode with a quartz absorbance microcuvette (1 cm pathlength). The spectral range for all absorbance measurements was from 230-1100 nm to ensure that both the UV and NIR absorption, from proteins and ICG respectively, were recorded.

The spectral features of ICG provide insight into the conformational states of ICG present within NETs. ICG can be in either a monomeric form, indicated by an absorption peak at 805 nm, or in an H-like aggregated form [73, 74], indicated by a secondary absorption peak at 740 nm. We define the parameter  $\psi$  as the ratio of the monomeric ICG absorbance to that of the H-like aggregate form of ICG. We note that the “absorption” of NETs is effectively a combination of optical scattering and photon absorption. Therefore, the spectra of EGs (formed using 0  $\mu$ M ICG in the loading buffer) contains both the optical scattering component of the particles, as well as the absorption component of proteins and any residual hemoglobin. To calculate  $\psi$ , we first removed the contribution of optical scattering and absorption by other components in NETs by subtracting the baseline absorption spectrum of EGs (constructs without ICG) from each absorption spectrum of NETs. Then, we used this baseline-subtracted absorbance for the calculation of  $\psi$ , as follows:

$$\psi = \frac{A^*(\lambda = 805 \text{ nm})}{A^*(\lambda = 740 \text{ nm})} \quad (1)$$

where  $A^*(\lambda = 805 \text{ nm})$  is the absorbance value of NETs at 805 nm minus the absorbance value of EGs at 805 nm. Similarly,  $A^*(\lambda = 740 \text{ nm})$  is the absorbance value of NETs at 740 nm minus the absorbance value of EGs at 740 nm. Wavelength is denoted as  $\lambda$ .

### G. Quantification of ICG Loading Efficiency of NETs

We define the ICG loading efficiency ( $\varepsilon$ ) of NETs as:

$$\varepsilon = 1 - \frac{m_{\text{super}}}{m_{\text{initial}}} \quad (2)$$

where  $m_{\text{initial}}$  is the amount of ICG introduced into the loading buffer, and  $m_{\text{super}}$  is the amount of ICG present in the

supernatant upon completing the fabrication of NETs. The supernatant was collected immediately after centrifugation and stored in a dark refrigerator at 4°C to prevent ICG photobleaching. Supernatant solutions were contained in disposable polystyrene cuvettes (1 cm pathlength), and their absorption spectra (400-1100 nm) were obtained using the UV-Vis-NIR spectrophotometer. To determine  $m_{\text{super}}$ , we compared the absorbance value of the supernatant at its spectral peak (780 nm) to a calibration curve (data not shown) that related peak absorbance values of supernatant ICG to known concentrations of ICG in the same supernatant buffer.

Currently, the clinical formulation of ICG is free ICG dissolved in water. In order to compare the optical absorption of NETs with that of free ICG in water, we determined the equivalent concentration of free ICG that would have the same monomer absorbance value as each of the NETs formulations fabricated using various ICG concentrations in the loading buffer. To do this, we first subtracted the baseline spectrum of EGs (i.e., particles not loaded with ICG) from the absorption spectrum of each formulation of NETs. In this manner, we eliminated the contribution of optical scattering and protein absorption from each spectrum. We then compared the monomeric absorption peaks of baseline-subtracted NETs to a calibration curve of the monomeric absorption peaks of free ICG dissolved in water, in the range of  $\approx 1$ -26  $\mu\text{M}$ , to determine the equivalent free ICG concentration of NETs.

#### H. Excitation-Emission Mapping of NETs Fluorescence

To determine the fluorescence characteristics of each formulation of NETs, we mapped the excitation-emission (ExEm) spectra using a Fluorolog-3 spectrofluorometer (HORIBA, Ltd., Edison, New Jersey, USA). Solution of NETs were contained within a quartz cuvette (1 cm pathlength). The excitation wavelengths ranged between 600-830 nm, and were generated using a 450 W xenon arc lamp. Corresponding to each excitation wavelength, the bathochromic fluorescence light was collected by the detector to ensure the collection of only the fluorescence, but not the scattered light.

Prior to ExEm mapping, a sample of each NETs formulation was diluted to have a NIR peak absorbance of 0.2 or lower. To correct for the primary inner-filter effect, which arises from the attenuation of excitation light in strongly absorbing samples [75], the fluorescence intensity values ( $f$ ) in each ExEm map were normalized with respect to the percentage of excitation light absorbed by the sample, as:

$$F(\lambda_{\text{ex}}, \lambda_{\text{em}}) = \frac{f(\lambda_{\text{ex}}, \lambda_{\text{em}})}{1 - 10^{-A_{\text{ex}}}} \quad (3)$$

where  $F(\lambda_{\text{ex}}, \lambda_{\text{em}})$  is the normalized fluorescence emission,  $\lambda_{\text{ex}}$  is a given excitation wavelength,  $\lambda_{\text{em}}$  is an emission wavelength in response to excitation at  $\lambda_{\text{ex}}$ , and  $A_{\text{ex}}$  is the absorbance of the diluted NETs formulation at  $\lambda_{\text{ex}}$ .

To obtain an estimate of total fluorescence emission for a given NETs formulation, we integrated the emission in response to two bands of excitation wavelengths, 656-678 nm and 745-779 nm. These bands correspond to the excitation light sources utilized in a clinically relevant NIR intraoperative fluorescence imaging system, the

Fluorescence-Assisted Resection and Exploration (FLARE) system [17]. We chose this system as an example since its optical specifications needed for our analyses are readily available in published scientific literature [17]. The system consists of two LED sources for excitation in bands of 656-678 nm and 745-779 nm. Fluorescence emission is passed through two NIR filters with respective bandpass wavelengths of 689-725 nm and 800-848 nm. Mathematically, we define  $\gamma$ , the integrated normalized fluorescence emission, as:

$$\begin{aligned} \gamma = & \sum_{\lambda_{\text{ex}} = 656 \text{ nm}}^{\lambda_{\text{ex}} = 678 \text{ nm}} \left[ \int_{\lambda_{\text{em}} = 689 \text{ nm}}^{\lambda_{\text{em}} = 725 \text{ nm}} F(\lambda_{\text{ex}}, \lambda_{\text{em}}) d\lambda_{\text{em}} \right] \\ & + \sum_{\lambda_{\text{ex}} = 656 \text{ nm}}^{\lambda_{\text{ex}} = 678 \text{ nm}} \left[ \int_{\lambda_{\text{em}} = 800 \text{ nm}}^{\lambda_{\text{em}} = 848 \text{ nm}} F(\lambda_{\text{ex}}, \lambda_{\text{em}}) d\lambda_{\text{em}} \right] \\ & + \sum_{\lambda_{\text{ex}} = 745 \text{ nm}}^{\lambda_{\text{ex}} = 779 \text{ nm}} \left[ \int_{\lambda_{\text{em}} = 800 \text{ nm}}^{\lambda_{\text{em}} = 848 \text{ nm}} F(\lambda_{\text{ex}}, \lambda_{\text{em}}) d\lambda_{\text{em}} \right] \end{aligned} \quad (4)$$

We also determined the relative fluorescence quantum yield ( $\phi_{\text{NETs}}$ ) for each of the NETs formulations in response to 780 nm excitation wavelength, which corresponds to the absorption peak of free ICG, as:

$$\begin{aligned} \phi_{\text{NETs}}(\lambda_{\text{ex}} = 780 \text{ nm}) &= \phi_{\text{ICG}}(\lambda_{\text{ex}} = 780 \text{ nm}) \\ &\times \left[ \frac{\int_{\lambda_{\text{em}} = 800 \text{ nm}}^{\lambda_{\text{em}} = 850 \text{ nm}} f_{\text{NETs}}(\lambda_{\text{ex}} = 780 \text{ nm}, \lambda_{\text{em}}) d\lambda_{\text{em}}}{1 - 10^{-A_{\text{NETs}}(\lambda_{\text{ex}} = 780 \text{ nm})}} \right] \\ &\times \left[ \frac{1 - 10^{-A_{\text{ICG}}(\lambda_{\text{ex}} = 780 \text{ nm})}}{\int_{\lambda_{\text{em}} = 800 \text{ nm}}^{\lambda_{\text{em}} = 850 \text{ nm}} f_{\text{ICG}}(\lambda_{\text{ex}} = 780 \text{ nm}, \lambda_{\text{em}}) d\lambda_{\text{em}}} \right] \end{aligned} \quad (5)$$

where  $\phi_{\text{ICG}}(\lambda_{\text{ex}} = 780 \text{ nm})$  is the fluorescence quantum yield ( $\approx 2.58\%$ ) [52] of free ICG in water (6.45  $\mu\text{M}$ ) at 780 nm excitation wavelength,  $f_{\text{NETs}}(\lambda_{\text{ex}} = 780 \text{ nm}, \lambda_{\text{em}})$  is the fluorescence emission intensity of a given NETs formulation in response to 780 nm excitation,  $A_{\text{NETs}}(\lambda_{\text{ex}} = 780 \text{ nm})$  is the absorbance value of a given NETs formulation at 780 nm,  $A_{\text{ICG}}(\lambda_{\text{ex}} = 780 \text{ nm})$  is the absorbance value of free ICG in water (6.45  $\mu\text{M}$ ) at 780 nm, and  $f_{\text{ICG}}(\lambda_{\text{ex}} = 780 \text{ nm}, \lambda_{\text{em}})$  is the fluorescence emission intensity of free ICG in water (6.45  $\mu\text{M}$ ) in response to 780 nm excitation wavelength.

#### I. Determination of NETs Fluorescence Stability at 4 °C and 37 °C

We investigated the fluorescence stability of the three types of NETs fabricated using 20  $\mu\text{M}$  ICG stored at either 4 °C or 37 °C for up to 12 hours. Following a given storage time  $t$ , each sample of NETs, suspended in 1X PBS, was photo-excited at 780 nm. The normalized fluorescence emission [see (3)] at a given  $t$  was integrated to yield the quantity  $I(t)$  as:



$$I(t) = \int_{\lambda_{em}=795 \text{ nm}}^{\lambda_{em}=900 \text{ nm}} F(\lambda_{ex}=780 \text{ nm}, \lambda_{em}) d\lambda_{em} \quad (6)$$

We define  $I^*$  as the value of  $I$  normalized to its initial value at  $t = 0$  (immediately after fabrication).

### III. RESULTS AND DISCUSSION

#### A. Hydrodynamic Diameter and Zeta Potential ( $\zeta$ ) of NETs

Based on the dynamic light scattering (DLS) method, the mean intensity-weighted average (z-average) diameter of  $\mu$ NETs ranged between  $\approx 1.9$ - $2.1 \mu\text{m}$ , depending on the ICG concentration used in the loading buffer [Fig. 2(a)]. When  $\mu$ NETs were fabricated using ICG loading concentrations in the range of 5-100  $\mu\text{M}$ , the resulting diameters were significantly larger ( $p < 0.01$ ) than that of micrometer-sized erythrocyte ghosts ( $\mu$ EGs). However, diameters of  $\mu$ NETs approached a plateau level of  $\approx 2.1 \mu\text{m}$  for ICG loading concentrations  $\geq 20 \mu\text{M}$ .

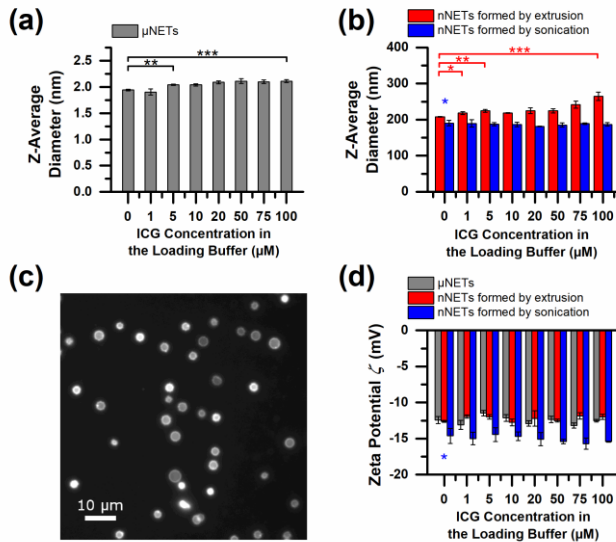


Fig. 2. Size and zeta potential of NETs. z-average diameters were estimated by dynamic light scattering (DLS) for: (a)  $\mu$ EGs and  $\mu$ NETs, and (b) nEGs and nNETs. (c) Fluorescence image of  $\mu$ NETs (100X magnification) formed using 20  $\mu\text{M}$  ICG in the loading buffer. (d) Zeta potential ( $\zeta$ ) of EGs and NETs in 1X ( $\approx 300$  mOsm) phosphate-buffered saline (PBS). Single, double, and triple asterisks indicate statistically significant differences with  $p < 0.05$ , 0.01, and 0.001 respectively. In panel (d), the single blue asterisk indicates statistically significant differences between the  $\zeta$  values of nEGs formed by sonication, compared to the  $\zeta$  values of the other two types of NETs.

nNETs formed by extrusion also had significantly larger diameters compared to nEGs formed by extrusion, as shown in Fig. 2(b). Depending on the ICG concentration in the loading buffer, z-average diameters of nNETs formed by extrusion ranged between  $\approx 203$ - $255$  nm. We have previously published SEM [56] and TEM [55] images of extruded nNETs. In these papers, we have also demonstrated that the electron microscope- and DLS-based measurements of nNETs diameters are in agreement. Estimates of  $\mu$ NETs diameter based on fluorescence microscopy [Fig. 2(c)] are also in agreement with DLS-based estimates in Fig. 2(a). We attribute

the increase in diameter of  $\mu$ NETs and nNETs formed by extrusion with increased ICG loading concentration to the incorporation of ICG molecules into the phospholipid membrane of NETs. Such localization of the dye may increase the overall diameter of the constructs. Indeed, fluorescence microscopy of  $\mu$ NETs revealed partial localization of ICG to the membrane periphery [Fig. 2(c)].

The z-average diameters of nNETs formed by sonication are smaller than the diameter of nNETs formed by extrusion [Fig. 2(b)]. The mean diameters of nNETs formed by sonication ranged between  $\approx 181$ - $190$  nm, and unlike  $\mu$ NETs and nNETs formed by extrusion, did not show a statistically significant dependence on ICG loading concentration. This result suggests that ICG may be primarily localized in the interior of nNETs formed by sonication rather than being embedded within the phospholipid membrane. We attribute this to the disruption and weakening of the membrane and cytoskeleton of EGs during sonication, which may be the physical basis for localization of ICG to the interior cavity.

The  $\zeta$  values for  $\mu$ NETs and nNETs formed by extrusion were indistinguishable from the  $\zeta$  of untreated bovine RBCs, which was measured to be  $-12.78 \pm 0.84$  mV in 1X PBS ( $\approx 300$  mOsm) [Fig. 2(d)]. These results suggest that glycophorin A, and sialic acid, the primary negative charge-bearing components of the RBC membrane [76], were not removed by hypotonic treatment or mechanical extrusion.

Maintaining the normal  $\zeta$  of RBCs can be a contributing factor in increasing the circulation time of NETs. Gbadamosi et al. found a linear relationship between the  $\zeta$  of methoxyl poly(ethylene glycol)-coated polystyrene microspheres and their uptake by mouse macrophages [77]. Extrapolation of their data shows that  $\zeta$  of approximately  $-15$  mV would result in none or minimal uptake by phagocytes. This value is remarkably close to the  $\zeta$  value of mouse [78] and human RBCs [78, 79]. Therefore, NETs and other particle systems with similar  $\zeta$ , may be minimally uptaken by macrophages as compared to neutral or highly charged particles [80, 81].

All formulations of nNETs formed by sonication had  $\zeta$  values that were significantly lower ( $p < 0.05$ ) than the  $\zeta$  of bovine RBCs,  $\mu$ NETs, and nNETs fabricated by extrusion. This may be due to degradation of sialic acid residues or membrane surface proteins during sonication. For the three types of NETs, there were no statistically significant changes in  $\zeta$  values in response to changes in the ICG concentration within the loading buffer [Fig. 2(d)]. This result suggests that the sulfonate portions of ICG, which are responsible for the negative charge of ICG, were completely encapsulated (either localized within the interior cavity or embedded within the membrane) [43], and not exposed to the external environment of the erythrocyte-derived constructs.

Using DLS, Kuo et al. demonstrated that suspensions of nEGs formed by sonication did not aggregate despite freeze-thaw cycling up to five cycles [82]. This result was in contrast to liposomal formulations that aggregated after the first freeze-thaw cycle [82]. Our own studies demonstrated that the diameter and  $\zeta$  of nNETs formed by extrusion did not change even after eight weeks of storage at  $-20^\circ\text{C}$  [83]. Therefore, cryopreservation may serve as a suitable method for the long-

term storage of nNETs since the particles remain colloiddally stable after freeze-thaw cycling.

### B. Absorption characteristics of NETs

The absorption spectra of  $\mu$ NETs, nNETs formed by extrusion, and nNETs formed by sonication revealed NIR peaks that were centered between 801-805 nm, 797-802 nm, and 799-802 nm, respectively (Fig. 3). These spectral peaks are attributed to the monomer form of ICG, as indicated in previous studies [54-56], and were bathochromically shifted with respect to the absorption peak of free ICG (780 nm) by approximately 20 nm. This shift is consistent with the behavior of ICG in emulsions and micellar formulations [52, 84], and can be attributed to the intercalation of ICG into the lipid bilayer of NETs and binding to the phospholipids and membrane proteins therein [43, 55, 84], leading to changes in the conformation of ICG and its electronic states.

The absorption shoulder in the spectral range of 720-760 nm corresponds to the H-like aggregate form of ICG [54, 74].

This sandwich-like,  $\pi$ - $\pi$  stacking of individual ICG molecules results in interaction of the individual transition dipole moments that raises the excited-state energy to produce a blue-shifted absorption peak [49, 73, 74]. In water, even relatively low concentrations of ICG ( $> 10 \mu\text{M}$ ) will begin to form H-aggregates [74, 85].

As the ICG concentration in the loading buffer increased, there was a corresponding non-linear increase in ICG absorption in the range of 600-900 nm for the three types of NETs. For example, for  $\mu$ NETs [Fig. 3(a)], doubling the concentration of ICG in the loading buffer, from 50-100  $\mu\text{M}$ , resulted in an increase in peak NIR absorbance of only 9.4%. For nNETs formed by extrusion [Fig. 3(b)], the peak NIR absorbance only increased 27.8% in response to the same increase of 50-100  $\mu\text{M}$  ICG in the loading buffer. For nNETs formed by sonication, this same increase in ICG loading buffer did not change the absorption spectrum [Fig. 3(c)]. This result suggests that there is a limit to the amount of ICG that can be loaded into NETs. Nevertheless, the nNETs formed by

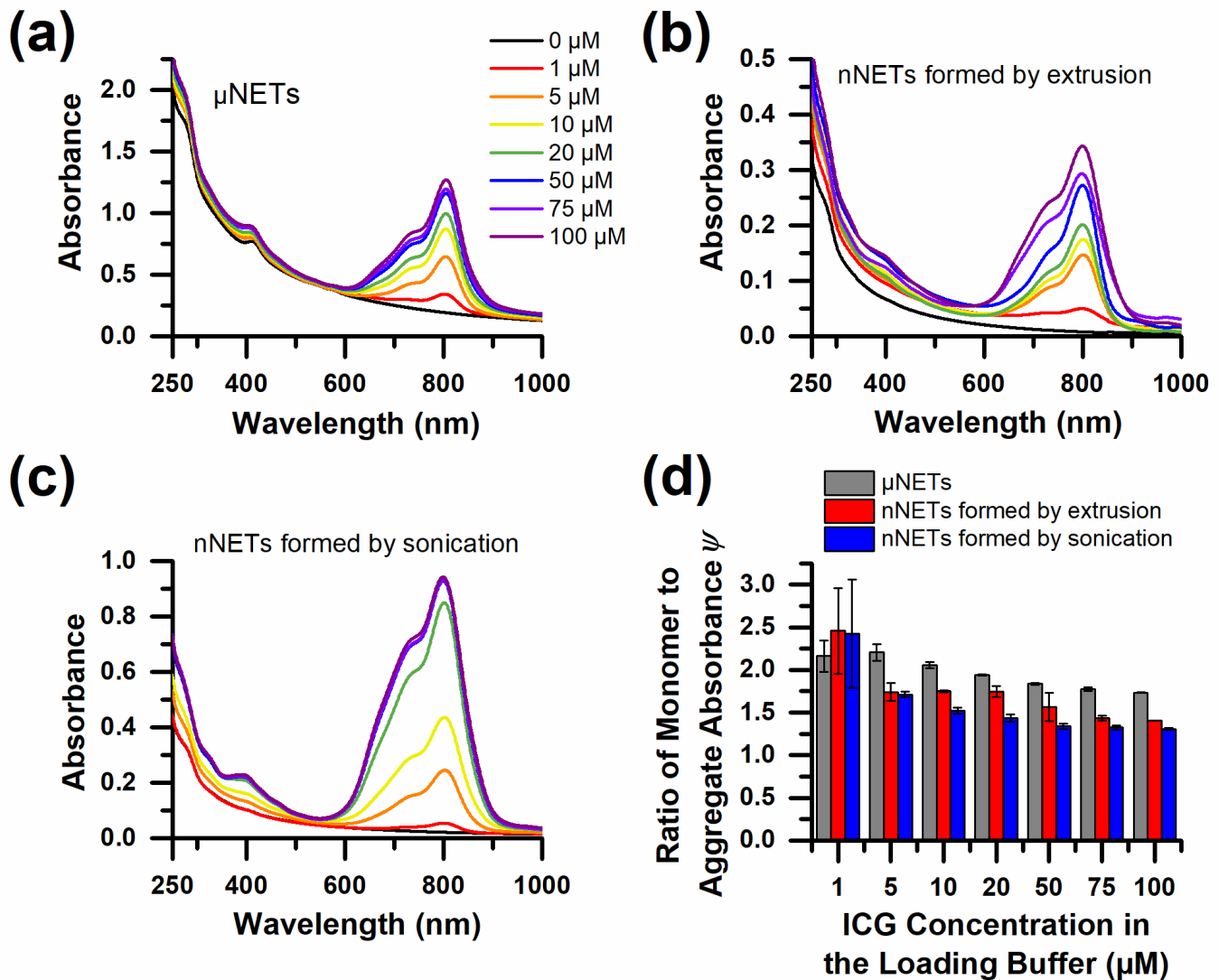


Fig. 3. Optical absorption characteristics of NETs. UV-Vis-NIR absorption spectra of: (a)  $\mu$ EGs and  $\mu$ NETs, (b) nEGs and nNETs formed by extrusion, and (c) nEGs and nNETs formed by sonication. In panel (d), we present the ratio of the monomer to H-like aggregate absorbance values of ICG ( $\psi$ ) [see (1)] for NETs formed using various concentrations of ICG in the loading buffer. The displayed legend (0-100  $\mu\text{M}$ ) corresponds to the ICG concentration in the loading buffer to fabricate the three types of NETs and is shared among panels (a), (b), and (c). Each displayed absorption spectrum in panels (a), (b), and (c) is an average of triplicate samples. Error bars in panel (d) are the SDs associated with the triplicate samples of each formulation.

sonication had the highest absorption in the range of 600-900 nm, suggestive of higher loading efficiency of ICG into these nNETs. We present quantitative data regarding ICG loading efficiency in the following section.

Optical attenuation over the spectral band of 250-500 nm is in part due to scattering by the erythrocyte-derived particles, and absorption by proteins at 280 nm. The presence of ICG also makes small contributions to absorbance values at 280 nm, and 400 nm (data not shown). Despite having nearly the same amount of phospholipid membrane material as  $\mu$ NETs, nNETs formed by sonication showed less attenuation in the 250-500 nm band, owing to their smaller diameter [Fig. 3(c)]. In a previous study, we showed that the reduced scattering coefficient of nNETs was less than half ( $\approx 45\%$ ) of that of  $\mu$ NETs [54], which is consistent with the lower attenuation in the 250-500 nm spectral band for nNETs formed by sonication. nNETs formed by extrusion had even lower attenuation in this spectral band, due to loss of EG material during the extrusion process, resulting in fewer relative number of light-scattering particles. The lower amount of EG materials in the extruded type is also a contributing factor for their relatively low NIR absorbance and low ICG loading efficiency [Fig. 4(a)].

The parameter  $\psi$  provides a quantitative measure of the amount of ICG in its monomeric form relative to its H-like aggregate form within the NETs, as described by (1). Values of  $\psi$  decreased as the concentration of ICG in the loading buffer increased, indicating progressively higher fractions of the H-like aggregate forms of ICG were present in NETs [Fig. 3(d)]. The increase in H-like aggregate fractions within NETs is likely due to their presence in the ICG loading buffer prior to being loaded into NETs. At ICG loading concentrations of  $\geq 5 \mu\text{M}$ , values of  $\psi$  were highest for  $\mu$ NETs. Thus, the relative fractions of the monomeric form of ICG in  $\mu$ NETs was higher than those in nNETs formed by either sonication or extrusion. This behavior influences the fluorescence properties of NETs, as shown later in the text.

### C. ICG Loading efficiency of NETs and Equivalent Free-ICG Concentrations

We estimated the loading efficiencies of ICG into NETs ( $\varepsilon$ ) using (2). For all three types of NETs, there was a monotonic decrease in  $\varepsilon$  as the ICG concentration in the loading buffer was increased beyond  $1 \mu\text{M}$  [Fig. 4(a)]. The average value of  $\varepsilon$  for  $\mu$ NETs, and nNETs formed by extrusion or sonication methods were 87%, 94%, and 98% respectively when using  $1 \mu\text{M}$  ICG concentration in the loading buffer [Fig. 4(a)]. The low values of  $\varepsilon$  associated with use of higher concentrations of ICG can be attributed to the fixed amount of EG material available to accept ICG. At high loading concentrations of ICG, the fixed amount of EG material can only uptake a limited amount of ICG, leaving a large fraction of non-encapsulated ICG in the loading buffer.

Notably, nNETs formed by sonication had significantly higher  $\varepsilon$  values ( $p < 0.05$ ) for all ICG loading concentrations when compared to  $\varepsilon$  for  $\mu$ NETs, and nNETs formed by extrusion (except nNETs formed by extrusion using  $1 \mu\text{M}$  ICG loading concentration). This is likely the result of the aforementioned sonication-induced disruption of the

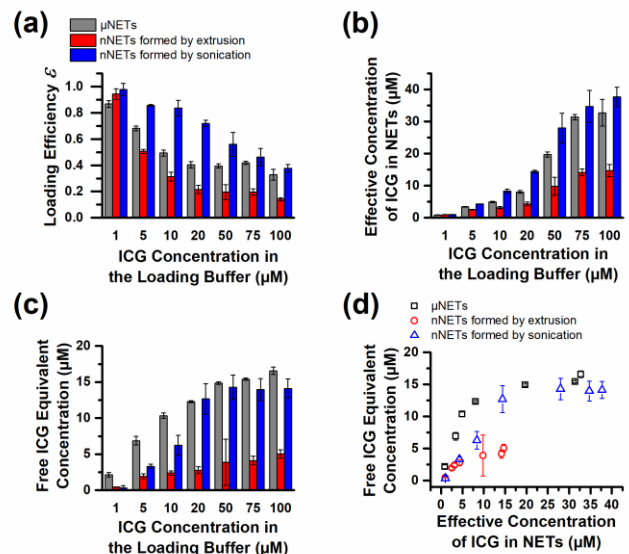


Fig. 4. ICG-loading characteristics of NETs. (a) ICG loading efficiency ( $\varepsilon$ ) into NETs [see (2)]. (b) Effective concentration of ICG within NETs. (c) Free ICG equivalent concentration of NETs as functions of ICG concentration of the loading buffer were determined by quantifying the amount of ICG in the supernatant. (d) The free ICG equivalent concentration corresponding to various effective concentrations of ICG within NETs. Error bars in each panel indicate the SDs associated with triplicate samples.

cytoskeletal network and membrane of EGs, which may allow ICG to be more readily loaded. The  $\varepsilon$  values for nNETs formed by extrusion were significantly lower ( $p < 0.05$ ) than those of other types of NETs, which may be attributed to the lower amount of EG material that remained after the extrusion process.

Multiplying  $\varepsilon$  by the concentration of ICG in the loading buffer yields the effective concentration of ICG within the population of NETs [Fig. 4(b)]. Thus, the effective concentration of ICG within NETs is an estimate of the concentration of ICG that would be dispersed in solution if NETs were disintegrated to release their ICG content. The effective concentration of ICG within NETs increased almost sigmoidally toward a maximum limit.

The maximum free ICG equivalent concentrations corresponding to  $\mu$ NETs, and nNETs formed by sonication or extrusion at various ICG loading concentrations were  $16.6 \pm 0.5$ ,  $14.1 \pm 1.3$ , and  $5.0 \pm 0.6 \mu\text{M}$ , respectively [Fig. 4(c)]. Much like the effective concentration of ICG within NETs, the asymptotic trend in free ICG equivalent concentration also indicated a maximum upper limit to the NIR absorbance of NETs.

Values of the free ICG equivalent concentration of NETs, as a function of the effective concentration ICG within NETs are presented in Fig. 4(d). These particular results provide a convenient method to quantitatively determine how the effective ICG concentration within NETs compares with various concentrations of free ICG dissolved in water. As the loaded concentration of ICG continued to increase beyond  $10 \mu\text{M}$  for nNETs fabricated by extrusion, and  $15 \mu\text{M}$  for  $\mu$ NETs and nNETs formed by sonication, there were nearly no further changes in the free ICG equivalent concentrations. This results suggests that at higher ICG loading concentrations, the additional ICG loaded into NETs was likely in the H-like aggregate form, and is consistent with the trend of lower  $\psi$



values when increasing the ICG concentration in loading buffer [see Fig. 3(d)].

#### D. Fluorescence Characteristics of NETs

Normalized excitation emission (ExEm) maps of NETs were calculated using (3) based on absorption and fluorescence spectral data, and are presented as Fig. 5. These maps are universal, and can be used by those who may be interested in using a given imaging system. Specifically, by utilizing these excitation and emission bands, one can select the appropriate NETs formulation suitable for fluorescence detection associated with a system of interest.

We attribute the emission “hot spots” in the range of  $\approx 770$ –830 nm to the monomeric forms of ICG within NETs. The most intense monomeric emissions were observed from  $\mu$ NETs and nNETs formed by sonication using 5  $\mu$ M ICG loading concentration when photo-excited at 778 nm and 780 nm, respectively. Interestingly, 5  $\mu$ M corresponded to the ICG concentration at which the maximum value of  $\psi$  for  $\mu$ NETs was determined [Fig. 3(d)]. nNETs formed by extrusion had the highest normalized fluorescence emission intensity value ( $F$ ) associated with monomeric ICG when they were fabricated using 20  $\mu$ M of ICG in the loading buffer and photo-excited at 780 nm [Fig. 5(b)].

A general trend associated with all three types of NETs is that increasing the concentration of ICG in the loading buffer beyond their respective values associated with maximum monomeric emission as indicated above, produced a second emission hot spot associated with the H-like aggregate emission. Peak values of  $F$  associated with H-like aggregate emissions were produced using respective ICG loading concentrations of 75, 75, and 100  $\mu$ M for  $\mu$ NETs, and nNETs formed by extrusion or sonication. The corresponding photo-

excitation wavelengths for these formulations were 678, 678, and 676 nm, respectively.

Using (4), we determined the formulations of NETs that generated maximum fluorescence emission for the detection bands used in the FLARE intraoperative imaging system [17]. To do this, we defined parameter  $\gamma$  as the integrated normalized emission collected over the excitation and emission wavelengths used by the system. The two excitation bands were 656–678 nm and 745–779 nm, whereas the two emission collection bands were 689–725 nm and 800–848 nm.

$\mu$ NETs with the highest average  $\gamma$  were fabricated using 10  $\mu$ M ICG in the loading buffer [Fig. 6(a)]. This formulation had a  $\gamma$  value that was statistically different from those associated with the 1 and 100  $\mu$ M ICG loading concentrations. nNETs formed by either extrusion or sonication had a maximum average  $\gamma$  when fabricated using 20  $\mu$ M ICG. We also determined that the maximal values of  $\gamma$  for the three types of NETs fabricated using 20  $\mu$ M ICG were not statistically different from each other. Therefore, the  $\gamma$  of  $\mu$ NETs and nNETs is effectively maximized when fabricating them using 20  $\mu$ M ICG in the loading buffer. The corresponding free ICG equivalent concentrations for these formulations were  $12.3 \pm 0.1$ ,  $2.8 \pm 0.5$ , and  $13 \pm 2$   $\mu$ M for  $\mu$ NETs, nNETs formed by extrusion, and nNETs formed by sonication [Fig. 4(c)].

Using (5), we determined the relative fluorescence quantum yield,  $\phi$ , of NETs in response to excitation at 780 nm, using 6.45  $\mu$ M ICG dissolved in water as the reference sample for quantum yield calculations [52]. The maximum values of  $\phi$  were 4.38%, 3.27%, and 2.98% for  $\mu$ NETs, nNETs formed by extrusion, and nNETs formed by sonication, respectively [Fig. 6(b)]. The ICG concentrations used to fabricate NETs with maximum  $\phi$  were 10, 10, and 1  $\mu$ M for  $\mu$ NETs, nNETs

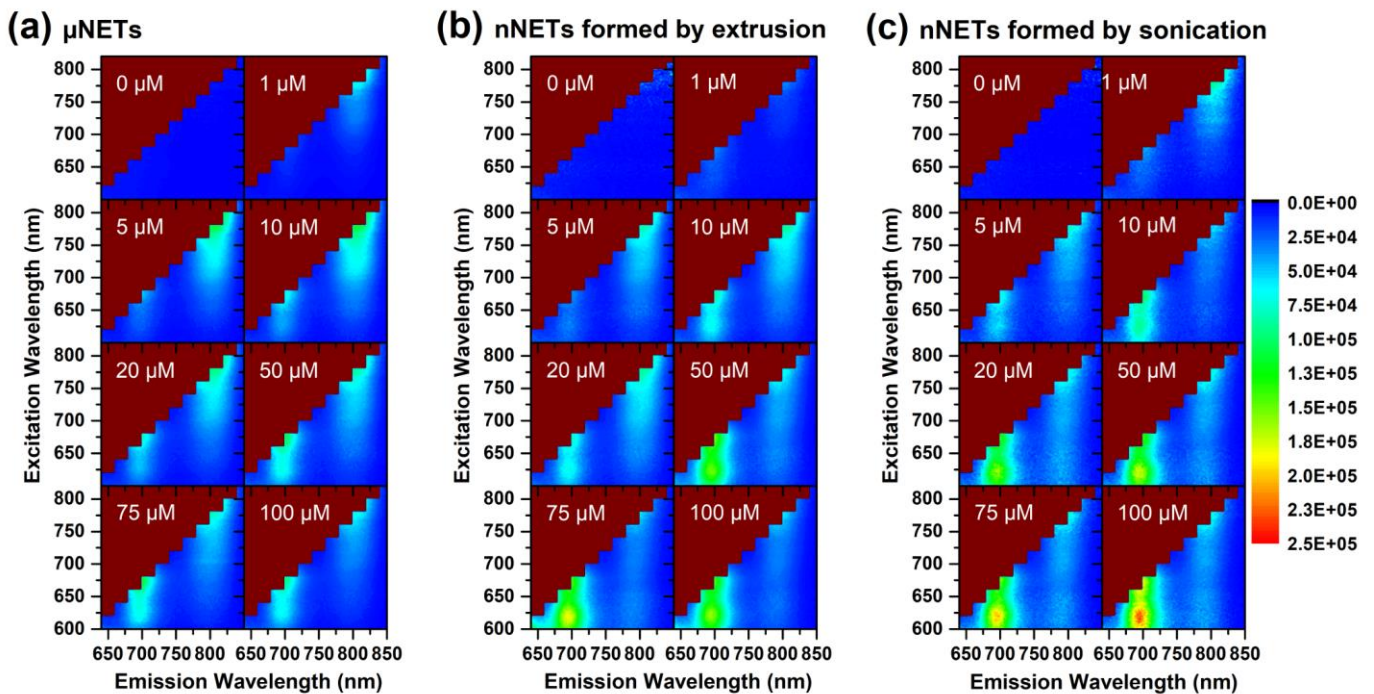


Fig. 5. Normalized excitation-emission (ExEm) maps for: (a)  $\mu$ NETs, (b) nNETs formed by extrusion, and (c) nNETs formed by sonication. NETs were fabricated using ICG concentrations in the range of 0–100  $\mu$ M. Each displayed ExEm map is an average of three ExEm maps generated using triplicate samples. The scale bar on the right corresponds to the values of  $F$ , [see (3)].

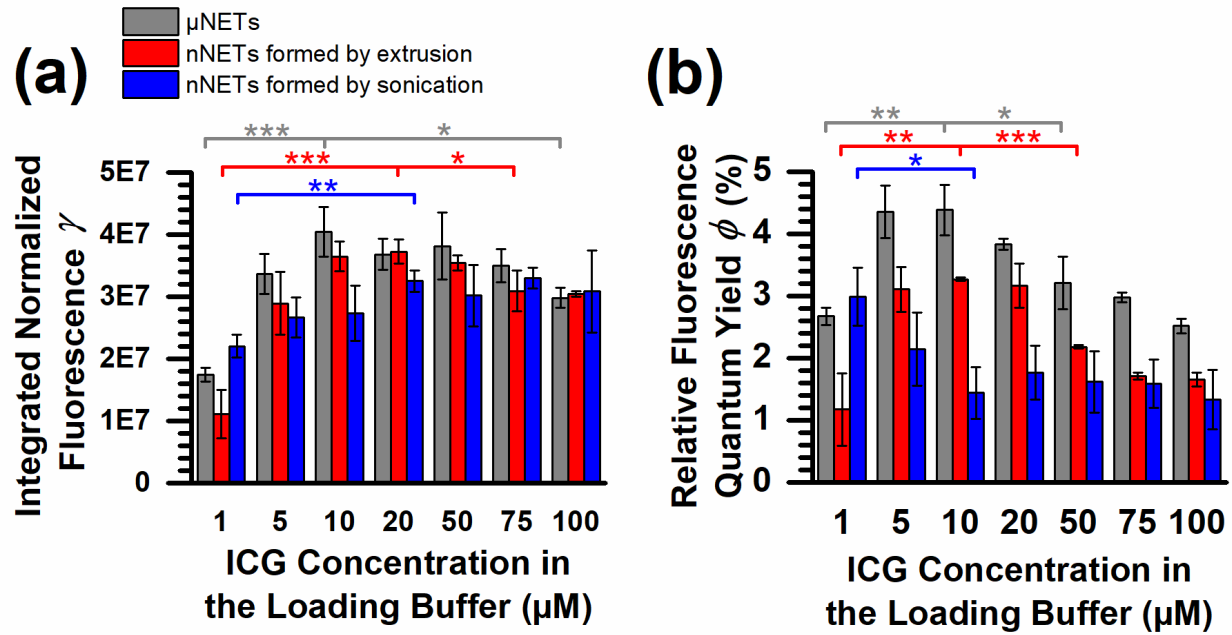


Fig. 6. Integrated normalized fluorescence emission [see (4)], and relative fluorescence quantum yield [see (5)] of NETs. (a) Values of the integrated normalized fluorescence emission,  $\gamma$ , and (b) relative fluorescence quantum yield,  $\phi$ , as a function of ICG concentration in the loading buffer for the three types of NETs. Values of  $\phi$  are calculated relative to the  $\phi$  of 6.45  $\mu\text{M}$  free ICG in water, in response to excitation at 780 nm. Single, double, and triple asterisks indicate differences of  $p < 0.05$ , 0.01, and 0.001, respectively. Error bars indicate the SDs associated with triplicate samples.

formed by extrusion, and nNETs formed by sonication, respectively. Encapsulation of ICG into NETs resulted in  $\phi$  values that were up to  $\approx 70$ , 27, and 16% higher than those for free ICG for  $\mu\text{NETs}$ , and nNETs formed by extrusion or sonication, respectively.

The increase in  $\phi$  upon encapsulation of ICG into NETs can be attributed to the change in the local environment of ICG. Free ICG has a low value of  $\phi$ , partly due to its flexible polyene bridge that can rotate and fold, providing multiple pathways for non-radiative decay and relaxation of its energy from the excited state [86, 87]. ICG, among other cyanine dyes, is also prone to aggregation and self-quenching [43, 88, 89], which can also reduce  $\phi$ . Physical association of ICG molecules with NETs constituents (e.g., phospholipids and membrane proteins) derived from erythrocytes can stabilize the polyene bridges and reduce the rate of vibrational relaxation from the excited state, which can lead to increased  $\phi$ .

#### E. Fluorescence Stability of NETs and Free ICG

After 12 hours of storage at 4  $^{\circ}\text{C}$ , there were no statistically significant changes in the values of  $I^*$  [see (6)] for the three types of NETs (Fig. 7a). However, free ICG showed  $\approx 50\%$  reduction in  $I^*$  after 12 hours of storage at 4  $^{\circ}\text{C}$ . Micron-sized and nano-sized NETs formed by extrusion did not show statistically significant changes in  $I^*$  after 12 hours of storage at 4  $^{\circ}\text{C}$  or 37  $^{\circ}\text{C}$  (Fig. 7a and b), indicating their fluorescence stability. NETs formed by sonication showed about 15% reduction in  $I^*$  after 12 hours of storage at 37  $^{\circ}\text{C}$  (Fig. 7b), suggesting that sonication may have resulted in formation of NETs with weakened membrane, leading to some ICG leakage or degradation over this time interval. In comparison, free ICG after four hours of storage showed 40% reduction in  $I^*$ , which was further increased to 50% after 12 hours. Finally, we

summarize some of the key optical and material properties of the three types of fluorescence-optimized NETs in Table I.

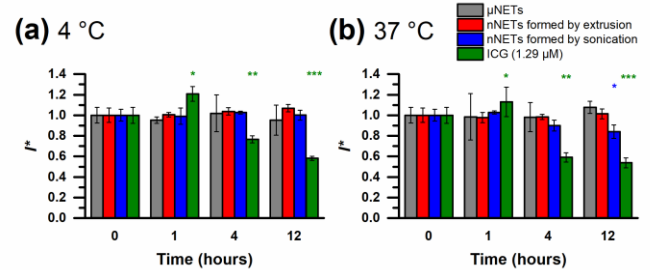


Fig. 7. Time-dependent fluorescence stability, quantified by the metric  $I^*$  [see (6)] for NETs and free ICG at (a) 4  $^{\circ}\text{C}$ , and (b) 37  $^{\circ}\text{C}$ . Error bars indicate normalized SD (SD divided by  $I(t = 0)$ ) for triplicate samples. Statistical significance is evaluated with respect to the initial values at  $t = 0$ . Single, double, and triple asterisks indicate differences of  $p < 0.05$ , 0.01, and 0.001, respectively. The excitation wavelength was 780 nm.

Type of NETs	z-average diameter (nm)	$\zeta$ (mV)	$\varepsilon$ (%)	$\phi$ (%)
$\mu\text{NETs}$	$2090 \pm 30$	$-12.9 \pm 0.4$	$40 \pm 2$	$3.8 \pm 0.1$
nNETs formed by extrusion	$225 \pm 8$	$-12.0 \pm 1.0$	$22 \pm 3$	$3.2 \pm 0.4$
nNETs formed by sonication	$181.1 \pm 0.5$	$-15.1 \pm 0.9$	$72 \pm 2$	$1.8 \pm 0.4$

For the z-average diameter and  $\zeta$ , the uncertainty values indicate the SD of triplicate samples, where each sample was measured eight times and averaged to obtain a single value. The uncertainty of the estimated  $\varepsilon$  and  $\phi$  values indicate the SD associated with a single measurement for triplicate samples.

#### IV. CONCLUSION

We have fabricated micrometer-sized NETs ( $\mu$ NETs), and nanometer-sized NETs (nNETs) formed by either mechanical extrusion or sonication of erythrocyte ghosts, and characterized several of their key material properties as a function of ICG loading concentration. We found that  $\mu$ NETs and nNETs formed by extrusion retained the zeta potential ( $\zeta$ ) of native erythrocytes ( $\approx -12$  mV in 1X PBS), whereas nNETs formed by sonication had a statistically significant decrease in  $\zeta$  ( $\approx -15$  mV in 1X PBS). This decrease in  $\zeta$  suggests alteration of charge-bearing moieties on the erythrocytes membrane (e.g., sialic acid or membrane proteins) due to the sonication process. Nevertheless,  $\zeta$  did not vary significantly with ICG concentration, suggesting that the negatively-charged ICG molecules were fully encapsulated within the three types of NETs. We determined that 20  $\mu$ M ICG utilized in fabricating NETs presents an optimal concentration that maximizes the integrated fluorescence emission for  $\mu$ NETs and nNETs despite statistically significant differences in their ICG loading efficiency when applied at this concentration. NETs fabricated using 20  $\mu$ M ICG had fluorescence quantum yields that were 70, 27, and 16% greater than that of free-ICG when encapsulated into in  $\mu$ NETs and nNETs formed by extrusion or sonication, respectively. We also determined that NETs had greater fluorescence stability as compared to free ICG at both 4  $^{\circ}$ C and 37  $^{\circ}$ C. These results can guide the engineering of NETs with maximal NIR fluorescence emission for specific biomedical imaging applications such as fluorescence-guided tumor resection, and real-time angiography.

#### REFERENCES

- [1] J. V. Frangioni. (2003, Oct.). In vivo near-infrared fluorescence imaging. *Curr. Opin. Chem. Biol.* [Online]. 7(5), pp. 626-634. Available: <https://www.doi.org/10.1016/j.cbpa.2003.08.007>
- [2] S. L. Gibbs. (2012, Sep.). Near infrared fluorescence for image-guided surgery. *Quant. Imaging Med. Surg.* [Online]. 2(3), pp. 177-187. Available: <https://www.doi.org/10.3978/j.issn.2223-4292.2012.09.04>
- [3] A. M. Smith, et al. (2009, Nov.). Bioimaging: second window for in vivo imaging. *Nat. Nanotechnol.* [Online]. 4(11), pp. 710-711. Available: <https://www.doi.org/10.1038/nnano.2009.326>
- [4] E. Hemmer, et al. (2016, Jan.). Exploiting the biological windows: current perspectives on fluorescent bioprobes emitting above 1000 nm. *Nanoscale Horiz.* [Online]. 1(3), pp. 168-184. Available: <https://www.doi.org/10.1039/c5nh00073d>
- [5] M. Z. Lin. (2011, Sep.). Beyond the rainbow: new fluorescent proteins brighten the infrared scene. *Nat. Methods* [Online]. 8(9), pp. 726-728. Available: <https://www.doi.org/10.1038/nmeth.1678>
- [6] D. E. Miller, et al. (1962, Feb.). Comparison of cardiac output determination by direct Fick method and dye-dilution method using indocyanine green dye and a cuvette densitometer. *J. Lab. Clin. Med.* [Online]. 59(2), pp. 345-350. Available: <https://www.doi.org/10.5555/uri:pii:0022214362900185>
- [7] F. Weis, et al. (2014, Feb.). Indocyanine green clearance as an outcome prediction tool in cardiac surgery: a prospective study. *J. Crit. Care* [Online]. 29(2), pp. 224-229. Available: <https://www.doi.org/10.1016/j.jcrc.2013.10.023>
- [8] C. Jochum, et al. (2006, Apr.). Quantitative liver function tests in donors and recipients of living donor liver transplantation. *Liver Transplant.* [Online]. 12(4), pp. 544-549. Available: <https://www.doi.org/10.1002/lt.20627>
- [9] S. Afonso, et al. (2009, Sep.). The use of indocyanine green in the evaluation of hepatic function before and after hepatic resection surgery. *Intensive Care Med.* 35, p. 130.
- [10] P. Mohnle, et al. (2012, Jul.). Indocyanine green clearance after cardiac surgery: the impact of cardiopulmonary bypass. *Perfusion* [Online]. 27(4), pp. 292-299. Available: <https://www.doi.org/10.1177/0267659112439596>
- [11] B. F. Hochheimer. (1971, Nov.). Angiography of retina with indocyanine green. *Arch. Ophthalmol.* [Online]. 86(5), pp. 564-565. Available: <https://www.doi.org/10.1001/archoph.1971.01000010566014>
- [12] M. D. Lima, et al. (1996, Feb.). Indocyanine green angiography of optic disc and peripapillary retina in glaucoma. *Invest. Ophthalmol. Visual Sci.* 37(3), p. 1007.
- [13] M. S. Fineman, et al. (2001, Mar.). Safety of indocyanine green angiography during pregnancy - a survey of the retina, macula, and vitreous societies. *Arch. Ophthalmol.* [Online]. 119(3), pp. 353-355. Available: <https://www.doi.org/10.1001/archoph.119.3.353>
- [14] M. Hope-Ross, et al. (1994, Mar.). Adverse Reactions Due to Indocyanine Green. *Ophthalmology* 101(3), pp. 529-533.
- [15] S. L. Chen, et al. (2006, Sep.-Oct.). Lymphatic mapping and sentinel node analysis: current concepts and applications. *CA-Cancer J. Clin.* [Online]. 56(5), pp. 292-309. Available: <https://www.doi.org/10.3322/canjclin.56.5.292>
- [16] T. Isei and H. Okamoto. (2008, Feb.). Fluorescence navigation with indocyanine green for sentinel lymph node biopsy in acral melanoma and genital extramammary Paget's carcinoma. *Ann. Surg. Oncol.* 15, pp. 58-59.
- [17] S. L. Troyan, et al. (2009, Oct.). The FLARE intraoperative near-infrared fluorescence imaging system: a first-in-human clinical trial in breast cancer sentinel lymph node mapping. *Ann. Surg. Oncol.* [Online]. 16(10), pp. 2943-2952. Available: <https://www.doi.org/10.1245/s10434-009-0594-2>
- [18] H. Abe, et al. (2011, Feb.). Indocyanine green fluorescence imaging system for sentinel lymph node biopsies in early breast cancer patients. *Surg. Today* [Online]. 41(2), pp. 197-202. Available: <https://www.doi.org/10.1007/s00595-009-4254-8>
- [19] J. M. Korn, et al. (2014, Apr.). Indocyanine green SPY elite-assisted sentinel lymph node biopsy in cutaneous melanoma. *Plast. Reconstr. Surg.* [Online]. 133(4), pp. 914-922. Available: <https://www.doi.org/10.1097/Prs.0000000000000006>
- [20] V. Pitsinis, et al. (2015, Dec.). Indocyanine green fluorescence mapping for sentinel lymph node biopsy in early breast cancer. *Surg. Oncol.* [Online]. 24(4), pp. 375-379. Available: <https://www.doi.org/10.1016/j.suronc.2015.10.002>
- [21] S. Siddighi, et al. (2014, Oct.). Indocyanine green for intraoperative localization of ureter. *Am. J. Obstet. Gynecol.* [Online]. 211(4), pp. 436.e1-436.e2. Available: <https://www.doi.org/10.1016/j.ajog.2014.05.017>
- [22] L. Boni, et al. (2015, Jul.). Clinical applications of indocyanine green (ICG) enhanced fluorescence in laparoscopic surgery. *Surg. Endosc.* [Online]. 29(7), pp. 2046-2055. Available: <https://www.doi.org/10.1007/s00464-014-3895-x>
- [23] J. T. Alander, et al. (2012, Apr.). A review of indocyanine green fluorescent imaging in surgery. *Int. J. Biomed. Imaging* [Online]. 2012, p. 940585. Available: <https://www.doi.org/10.1155/2012/940585>
- [24] H. Athiraman, et al. (2004, Jul.). Selective photothermal tissue interaction using 805-nm laser and indocyanine green in tissue welding. *J. X-Ray Sci. Technol.* [Online]. 12(2), pp. 117-126. Available: <https://content.iospress.com/articles/journal-of-x-ray-science-and-technology/xst00105>
- [25] X. H. Zheng, et al. (2011, Mar.-Apr.). Indocyanine green-containing nanostructure as near infrared dual-functional targeting probes for optical imaging and photothermal therapy. *Mol. Pharmaceutics* [Online]. 8(2), pp. 447-456. Available: <https://www.doi.org/10.1021/mp100301t>
- [26] C. Shirata, et al. (2017, Oct.). Near-infrared photothermal/photodynamic therapy with indocyanine green induces apoptosis of hepatocellular carcinoma cells through oxidative stress. *Sci. Rep.* [Online]. 7(1), p. 13958. Available: <https://www.doi.org/10.1038/s41598-017-14401-0>
- [27] A. A. Warn, et al. (1994, Mar.). Photodynamic therapy of subcutaneous and intraocular tumors using indocyanine green. *Invest. Ophthalmol. Visual Sci.* 35(4), p. 1924.
- [28] K. Urbanska, et al. (2002, Apr.). Indocyanine green as a prospective sensitizer for photodynamic therapy of melanomas. *Acta Biochim. Pol.* [Online]. 49(2), pp. 387-391. Available: [http://www.actabp.pl/pdf/2\\_2002/387.pdf](http://www.actabp.pl/pdf/2_2002/387.pdf)

- [29] M. Sawa, et al. (2004, Jun.). Application of femtosecond ultrashort pulse laser to photodynamic therapy mediated by indocyanine green. *Br. J. Ophthalmol.* [Online]. 88(6), pp. 826-831. Available: <https://www.doi.org/10.1136/bjo.2003.031047>
- [30] H. M. Seo, et al. (2016, Oct.). Effects of repetitive photodynamic therapy using indocyanine green for acne vulgaris. *Int. J. Dermatol.* [Online]. 55(10), pp. 1157-1163. Available: <https://www.doi.org/10.1111/ijd.13258>
- [31] C. B. Ortega, et al. (2018, Apr.-Jun.). The use of fluorescence angiography during laparoscopic sleeve gastrectomy. *J. Soc. Laparoendosc. Surg.* [Online]. 22(2), Available: <https://www.doi.org/10.4293/JSLs.2018.00005>
- [32] J. A. Carr, et al. (2018, Apr.). Shortwave infrared fluorescence imaging with the clinically approved near-infrared dye indocyanine green. *Proc. Natl. Acad. Sci. U. S. A.* [Online]. 115(17), pp. 4465-4470. Available: <https://www.doi.org/10.1073/pnas.1718917115>
- [33] J. Neumann, et al. (2018, Feb.). Noninvasive quantitative assessment of microcirculatory disorders of the upper extremities with 2D fluorescence optical imaging. *Clin. Hemorheol. Microcirc.* [Online]. Available: <https://www.doi.org/10.3233/CH-170321>
- [34] Y. Kawasaki, et al. (2018, Jan.). Usefulness of fluorescence vascular imaging for evaluating splenic perfusion. *Aust. N. Z. J. Surg.* [Online]. Available: <https://www.doi.org/10.1111/ans.14364>
- [35] A. Majlesara, et al. (2017, Mar.). Indocyanine green fluorescence imaging in hepatobiliary surgery. *Photodiagn. Photodyn. Ther.* [Online]. 17, pp. 208-215. Available: <https://www.doi.org/10.1016/j.pdpdt.2016.12.005>
- [36] A. V. DSouza, et al. (2016, Aug.). Review of fluorescence guided surgery systems: identification of key performance capabilities beyond indocyanine green imaging. *J. Biomed. Opt.* [Online]. 21(8), Available: <https://www.doi.org/10.1117/1.Jbo.21.8.080901>
- [37] T. Kim, et al. (2018, Apr.). Fluorescence molecular imaging systems for intraoperative image-guided surgery. *Appl. Spectrosc. Rev.* [Online]. 53(2-4), pp. 349-359. Available: <https://www.doi.org/10.1080/05704928.2017.1323311>
- [38] T. Desmettre, et al. (2000, Jul.-Aug.). Fluorescence properties and metabolic features of indocyanine green (ICG) as related to angiography. *Surv. Ophthalmol.* [Online]. 45(1), pp. 15-27. Available: [https://www.doi.org/10.1016/S0039-6257\(00\)00123-5](https://www.doi.org/10.1016/S0039-6257(00)00123-5)
- [39] M. A. Yaseen, et al. (2008, Dec.). In-vivo fluorescence imaging of mammalian organs using charge-assembled mesocapsule constructs containing indocyanine green. *Opt. Express* [Online]. 16(25), pp. 20577-20587. Available: <https://www.doi.org/10.1364/Oe.16.020577>
- [40] S. Keiding, et al. (1993, Nov.). Enhancement of unbound clearance of ICG by plasma proteins, demonstrated in human subjects and interpreted without assumption of facilitating structures. *J. Hepatol.* [Online]. 19(3), pp. 327-344. Available: [https://www.doi.org/10.1016/S0168-8278\(05\)80541-0](https://www.doi.org/10.1016/S0168-8278(05)80541-0)
- [41] P. Ott, et al. (1997, Sep.). Hepatic ICG removal in the pig depends on plasma protein and hematocrit: evidence of sinusoidal binding disequilibrium and unstirred water layer effects. *Hepatology* [Online]. 26(3), pp. 679-690. Available: <https://www.doi.org/10.1002/hep.510260321>
- [42] S. Yoneya, et al. (1998, Jun.). Binding properties of indocyanine green in human blood. *Invest. Ophthalmol. Visual Sci.* [Online]. 39(7), pp. 1286-1290. Available: <https://iovs.arvojournals.org/article.aspx?articleid=2162006>
- [43] J. C. Kraft and R. J. Y. Ho. (2014, Mar.). Interactions of indocyanine green and lipid in enhancing near-infrared fluorescence properties: the basis for near-infrared imaging in vivo. *Biochemistry* [Online]. 53(8), pp. 1275-1283. Available: <https://www.doi.org/10.1021/bi500021j>
- [44] M. A. Yaseen, et al. (2007, Nov.-Dec.). Stability assessment of indocyanine green within dextran-coated mesocapsules by absorbance spectroscopy. *J. Biomed. Opt.* [Online]. 12(6), Available: <https://www.doi.org/10.1117/1.2821423>
- [45] T. Fukasawa, et al. (2014, Apr.). Fabrication of ICG dye-containing particles by growth of polymer/salt aggregates and measurement of photoacoustic signals. *Chem. Lett.* [Online]. 43(4), pp. 495-497. Available: <https://www.doi.org/10.1246/cl.131088>
- [46] B. Bahmani, et al. (2014, Sep.). Functionalized polymeric nanoparticles loaded with indocyanine green as theranostic materials for targeted molecular near infrared fluorescence imaging and photothermal destruction of ovarian cancer cells. *Lasers Surg. Med.* [Online]. 46(7), pp. 582-592. Available: <https://www.doi.org/10.1002/lsm.22269>
- [47] B. S. Jung, et al. (2011, Feb.). Optical nano-constructs composed of genome-depleted bromo mosaic virus doped with a near infrared chromophore for potential biomedical applications. *ACS Nano* [Online]. 5(2), pp. 1243-1252. Available: <https://www.doi.org/10.1021/nn1028696>
- [48] B. S. Jung and B. Anvari. (2013, Aug.). Virus-mimicking optical nanomaterials: near infrared absorption and fluorescence characteristics and physical stability in biological environments. *ACS Appl. Mater. Interfaces* [Online]. 5(15), pp. 7492-7500. Available: <https://www.doi.org/10.1021/am401800w>
- [49] Y. Guerrero, et al. (2017, Jun.). Optical characteristics and tumor imaging capabilities of near infrared dyes in free and nano-encapsulated formulations comprised of viral capsids. *ACS Appl. Mater. Interfaces* [Online]. 9(23), pp. 19601-19611. Available: <https://www.doi.org/10.1021/acsami.7b03373>
- [50] H. S. Jeong, et al. (2013, Dec.). The effect of mannosylation of liposome-encapsulated indocyanine green on imaging of sentinel lymph node. *J. Liposome Res.* [Online]. 23(4), pp. 291-297. Available: <https://www.doi.org/10.3109/08982104.2013.801488>
- [51] L. Viitala, et al. (2016, May.). Photothermally triggered lipid bilayer phase transition and drug release from gold nanorod and indocyanine green encapsulated liposomes. *Langmuir* [Online]. 32(18), pp. 4554-4563. Available: <https://www.doi.org/10.1021/acs.langmuir.6b00716>
- [52] A. K. Kirchherr, et al. (2009, Mar.-Apr.). Stabilization of indocyanine green by encapsulation within micellar systems. *Mol. Pharmaceutics* [Online]. 6(2), pp. 480-491. Available: <https://www.doi.org/10.1021/mp8001649>
- [53] Y. Hwang, et al. (2017, Oct.). In vivo cellular-level real-time pharmacokinetic imaging of free-form and liposomal indocyanine green in liver. *Biomed. Opt. Express* [Online]. 8(10), pp. 4706-4716. Available: <https://www.doi.org/10.1364/BOE.8.004706>
- [54] J. M. Burns, et al. (2017, Jan.). Optical properties of biomimetic probes engineered from erythrocytes. *Nanotechnology* [Online]. 28(3), Available: <https://www.doi.org/10.1088/1361-6528/28/3/035101>
- [55] B. Bahmani, et al. (2013, Jul.). Erythrocyte-derived photo-theranostic agents: hybrid nano-vesicles containing indocyanine green for near imaging and therapeutic applications. *Sci. Rep.* [Online]. 3, p. 2180. Available: <https://www.doi.org/10.1038/srep02180>
- [56] J. T. Mac, et al. (2016, Apr.). Erythrocyte-derived nano-probes functionalized with antibodies for targeted near infrared fluorescence imaging of cancer cells. *Biomed. Opt. Express* [Online]. 7(4), pp. 1311-1322. Available: <https://www.doi.org/10.1364/boe.7.001311>
- [57] R. Vankayala, et al. (2018, Apr.). Erythrocyte-derived nanoparticles as a theranostic agent for near-infrared fluorescence imaging and thrombolysis of blood clots. *Macromol. Biosci.* [Online]. 18(4), Available: <https://www.doi.org/10.1002/mabi.201700379>
- [58] J. Burns, et al. (2018, Jul.). Erythrocyte-derived theranostic nanoplateforms for near infrared fluorescence imaging and photodestruction of tumors. *ACS Appl. Mater. Interfaces* [Online]. Available: <https://www.doi.org/10.1021/acsami.8b08005>
- [59] R. W. Flower and R. Kling. (2017, Apr.). Observation and characterization of microvascular vasomotion using erythrocyte mediated ICG angiography (EM-ICG-A). *Microvasc. Res.* [Online]. 113, pp. 78-87. Available: <https://www.doi.org/10.1016/j.mvr.2017.02.006>
- [60] R. Agrawal, et al. (2017, Jul.). Fluorescent dye labeling of erythrocytes and leukocytes for studying the flow dynamics in mouse retinal circulation. *J. Visualized Exp.* [Online]. (125), p. e55495. Available: <https://www.doi.org/10.3791/55495>
- [61] H. Ren, et al. (2017, Sep.). Oxygen self-enriched nanoparticles functionalized with erythrocyte membranes for long circulation and enhanced phototherapy. *Acta Biomater.* [Online]. 59, pp. 269-282. Available: <https://www.doi.org/10.1016/j.actbio.2017.06.035>
- [62] G. Wan, et al. (2018, Feb.). Nanoscaled red blood cells facilitate breast cancer treatment by combining photothermal/photodynamic therapy and chemotherapy. *Biomaterials* [Online]. 155, pp. 25-40. Available: <https://www.doi.org/10.1016/j.biomaterials.2017.11.002>
- [63] J. G. Piao, et al. (2014, Oct.). Erythrocyte membrane is an alternative coating to polyethylene glycol for prolonging the circulation lifetime of gold nanocages for photothermal therapy. *ACS Nano* [Online]. 8(10), pp. 10414-10425. Available: <https://www.doi.org/10.1021/nn503779d>
- [64] J. R. Peng, et al. (2017, Dec.). Erythrocyte-membrane-coated prussian blue/manganese dioxide nanoparticles as H<sub>2</sub>O<sub>2</sub>-responsive oxygen generators to enhance cancer chemotherapy/photothermal therapy. *ACS Appl. Mater. Interfaces* [Online]. 9(51), pp. 44410-44422. Available: <https://www.doi.org/10.1021/acsami.7b17022>



- [65] L. Rao, et al. (2017, Jan.). Erythrocyte membrane-coated upconversion nanoparticles with minimal protein adsorption for enhanced tumor imaging. *ACS Appl. Mater. Interfaces* [Online]. 9(3), pp. 2159-2168. Available: <https://www.doi.org/10.1021/acsami.6b14450>
- [66] P. A. Oldenborg, et al. (2000, Jun.). Role of CD47 as a marker of self on red blood cells. *Science* [Online]. 288(5473), pp. 2051-2054. Available: <https://www.doi.org/10.1126/science.288.5473.2051>
- [67] S. Acharya and S. K. Sahoo. (2011, Mar.). PLGA nanoparticles containing various anticancer agents and tumour delivery by EPR effect. *Adv. Drug Delivery Rev.* [Online]. 63(3), pp. 170-183. Available: <https://www.doi.org/10.1016/j.addr.2010.10.008>
- [68] S. D. Li and L. Huang. (2008, Jul.-Aug.). Pharmacokinetics and biodistribution of nanoparticles. *Mol. Pharmaceutics* [Online]. 5(4), pp. 496-504. Available: <https://www.doi.org/10.1021/mp800049w>
- [69] D. E. Koppel. (1972, Dec.). Analysis of macromolecular polydispersity in intensity correlation spectroscopy - method of cumulants. *J. Chem. Phys.* [Online]. 57(11), p. 4814. Available: <https://www.doi.org/10.1063/1.1678153>
- [70] J. C. Thomas. (1987, May). The determination of log normal particle size distributions by dynamic light scattering. *J. Colloid Interface Sci.* [Online]. 117(1), pp. 187-192. Available: [https://www.doi.org/10.1016/0021-9797\(87\)90182-2](https://www.doi.org/10.1016/0021-9797(87)90182-2)
- [71] A. Sze, et al. (2003, May.). Zeta-potential measurement using the Smoluchowski equation and the slope of the current-time relationship in electroosmotic flow. *J. Colloid Interface Sci.* [Online]. 261(2), pp. 402-410. Available: [https://www.doi.org/10.1016/S0021-9797\(03\)00142-5](https://www.doi.org/10.1016/S0021-9797(03)00142-5)
- [72] M. A. Islam. (2004, Aug.-Sep.). Einstein-Smoluchowski diffusion equation: a discussion. *Phys. Scr.* [Online]. 70(2-3), pp. 120-125. Available: <https://www.doi.org/10.1088/0031-8949/70/2-3/008>
- [73] M. Kasha. (1963, Sep.). Energy transfer mechanisms and molecular exciton model for molecular aggregates. *Radiat. Res.* [Online]. 20(1), pp. 55-71. Available: <https://www.doi.org/10.2307/3571331>
- [74] B. S. Jung, et al. (2014, Mar.-Apr.). Revisiting indocyanine green: effects of serum and physiological temperature on absorption and fluorescence characteristics. *IEEE J. Sel. Top. Quantum Electron.* [Online]. 20(2), pp. 149-157. Available: <https://www.doi.org/10.1109/Jstqe.2013.2278674>
- [75] A. V. Fonin, et al. (2014, Jul.). Fluorescence of dyes in solutions with high absorbance. Inner filter effect correction. *PLoS One* [Online]. 9(7), p. e103878. Available: <https://www.doi.org/10.1371/journal.pone.0103878>
- [76] E. H. Eylar, et al. (1962). Contribution of sialic acid to surface charge of the erythrocyte. *Journal of Biological Chemistry* [Online]. 237(6), pp. 1992-2000. Available: <http://www.jbc.org/content/237/6/1992.long>
- [77] J. K. Gbadamosi, et al. (2002, Dec.). PEGylation of microspheres generates a heterogeneous population of particles with differential surface characteristics and biological performance. *FEBS Lett.* [Online]. 532(3), pp. 338-344. Available: [https://www.doi.org/10.1016/S0014-5793\(02\)03710-9](https://www.doi.org/10.1016/S0014-5793(02)03710-9)
- [78] P. S. Munksgaard, et al. (2014, Jun.). Sialic acid residues are essential for cell lysis mediated by leukotoxin from aggregatibacter actinomycetemcomitans. *Infect. Immun.* [Online]. 82(6), pp. 2219-2228. Available: <https://www.doi.org/10.1128/iai.01647-14>
- [79] K. M. Jan and S. Chien. (1973, May). Role of surface electric charge in red blood cell interactions. *J. Gen. Physiol.* [Online]. 61(5), pp. 638-654. Available: <https://www.doi.org/10.1085/jgp.61.5.638>
- [80] S. W. Tan, et al. (2015). Cell or cell membrane-based drug delivery systems. *Theranostics* [Online]. 5(8), pp. 863-881. Available: <https://www.doi.org/10.7150/thno.11852>
- [81] R. R. Arvizo, et al. (2011, Sep.). Modulating pharmacokinetics, tumor uptake and biodistribution by engineered nanoparticles. *PLoS One* [Online]. 6(9), p. e24374. Available: <https://www.doi.org/10.1371/journal.pone.0024374>
- [82] Y. C. Kuo, et al. (2016, Jan.). Colloidal properties of nanoerythrocytes derived from bovine red blood cells. *Langmuir* [Online]. 32(1), pp. 171-179. Available: <https://www.doi.org/10.1021/acs.langmuir.5b03014>
- [83] J. C. Tang, et al., "Effect of freezing on erythrocyte-derived optical nanoprobe," in *Optics in the Life Sciences Congress*, San Diego, CA, 2017, p. OmTu2D.4.
- [84] J. M. Devoisselle, et al. (1998, Dec.). A preliminary study of the in vivo behaviour of an emulsion formulation of indocyanine green. *Lasers Med. Sci.* [Online]. 13(4), pp. 279-282. Available: <https://www.doi.org/10.1007/s101030050008>
- [85] H. von Berlepsch and C. Bottcher. (2015, Sep.). H-aggregates of an indocyanine Cy5 dye: transition from strong to weak molecular coupling. *J. Phys. Chem. B* [Online]. 119(35), pp. 11900-11909. Available: <https://www.doi.org/10.1021/acs.jpcc.5b05576>
- [86] G. S. Hong, et al. (2011, Apr.). Near-infrared-fluorescence-enhanced molecular imaging of live cells on gold substrates. *Angew. Chem., Int. Ed.* [Online]. 50(20), pp. 4644-4648. Available: <https://www.doi.org/10.1002/anie.201100934>
- [87] R. C. Benson and H. A. Kues. (1977, Oct.). Absorption and fluorescence properties of cyanine dyes. *J. Chem. Eng. Data* [Online]. 22(4), pp. 379-383. Available: <https://www.doi.org/10.1021/je60075a020>
- [88] N. G. Zhegalova, et al. (2014, Sep.-Oct.). Minimization of self-quenching fluorescence on dyes conjugated to biomolecules with multiple labeling sites via asymmetrically charged NIR fluorophores. *Contrast Media Mol. Imaging* [Online]. 9(5), pp. 355-362. Available: <https://www.doi.org/10.1002/cmmi.1585>
- [89] U. Rosch, et al. (2006, Oct.). Fluorescent H-aggregates of merocyanine dyes. *Angew. Chem., Int. Ed.* [Online]. 45(42), pp. 7026-7030. Available: <https://www.doi.org/10.1002/anie.200602286>